RESEARCH ARTICLE

Evidence of active magmatic rifting at the Ma'Alalta volcanic field (Afar, Ethiopia)

Gianmaria Tortelli[1,2] · Anna Gioncada[1] · Carolina Pagli[1] · Mauro Rosi[1] · Laura De Dosso[1] · Derek Keir[2,3]

Abstract

During continental rifting, strain and magmatism are believed to localize to narrow magmatic segments, while the rift margin is progressively abandoned. We integrate volcanological, geochemical, petrological and seismic data from the Ma'Alalta volcanic field (MVF) near the western margin of Afar, to show that the MVF is an active magmatic segment. Magmatism in MVF initiated with lava flows and large-volume, caldera-forming ignimbrites from a central edifice. However, the most recent magmatic activity shifted towards mafic lava fields, cinder cones and obsidian-rich silicic domes erupted from vents aligned NNW-SSE, defining a ~ 35-km-long magmatic segment. Along the same area, a NNW-SSE alignment of earthquakes was recorded by two local seismic networks (2005–2009 and 2011–2013). The geochemistry of the mafic rocks is similar to those of nearby axial volcanoes. Inferred magma storage depth from mineral geobarometry shows that a shallow, silicic chamber existed at ~ 5-km depth below the stratovolcano, while a stacked plumbing system with at least three magma storage levels between 9 and 24 km depth fed the recent basalts. We interpret the wide set of observations from the MVF as evidence that the area is an active magmatic segment, showing that localised axial extension can be heavily offset towards the rift margin.

Keywords Ma'Alalta volcanic field · Rift segment · Central volcano · Tectonic extension · Rift margin · Magma plumbing

Introduction

The Ma'Alalta volcanic field (MVF hereafter) is located in Afar (Ethiopia), ~ 50 km north of Dabbahu volcano (Fig. 1). MVF consists of a felsic stratovolcano with summit nested calderas surrounded by more recent mafic lava flows and

Highlights
- Transition from caldera-forming to rift segment volcanism at MVF in Afar
- Types of eruptions, magma composition and storage depth change in time at MVF
- Parallel rift segments accommodate plate boundary extension
- Active rift segments can be offset towards the rift margin

✉ Gianmaria Tortelli
gianmaria.tortelli@unifi.it

1   Dipartimento di Scienze della Terra, Università di Pisa, Via Santa Maria, 53, 56126 Pisa, Italy

2   Dipartimento di Scienze della Terra, Università di Firenze, Via La Pira, 4, 50121 Florence, Italy

3   School of Ocean and Earth Science, University of Southampton, European Way, Southampton SO14 3ZH, UK

scoria cones and felsic lava flows and domes. Due to its location at the edge of the Afar depression, the MVF was originally classified as a marginal unit (Barberi et al. 1974a; Wiart and Oppenheimer 2005). However, little is known about the petrology, geochemistry and tectonics of MVF and how they relate to the tectonics of continental breakup in Afar.

The Afar rift is a triple junction where the Main Ethiopian Rift, Red Sea and the Gulf of Aden rift arms meet. Volcanism in Afar initiated ~ 30 Ma ago and was initially dominated by flood basalts (Hofmann et al. 1997). Since at least ~ 1 Ma, active rifting and volcanism have focused to en-echelon axial magmatic segments (~ 70-km-long, ~ 20-km-wide) marking the current plate boundary of the rift (e.g. Dabbahu segment, Manda Hararo segment and Erta Ale segment) (Fig. 1a) (Oppenheimer and Francis 1998; Wright et al. 2012; Medynski et al. 2013). Holocene rift marginal volcanism has also produced large volumes of lavas, such as those erupted by the silicic stratovolcanoes of the Nabro-Mallahle alignment (marginal volcanism) or from basaltic shield volcanoes, such as Dabbayra (transverse volcanism) (Fig. 1a). Nevertheless, despite the peculiarity of the marginal volcanism, current knowledge about marginal volcanoes, their magma sources and plumbing system and the relationships with

Fig. 1 a Regional tectonic map showing the three diverging plates (Nubia, Arabia and Somalia) and the main structures. In red the magmatic segments and in green marginal volcanoes (triangles) and transverse structures (segments). E-A, Erta Ale; MH, Manda Hararo; Da$_s$, Dabbahu segment; Na, Nabro; Du, Dubbi; As, Assab range; Db, Dabbayra; MER, Main Ethiopian Rift; GoA, Gulf of Aden; RS, Red Sea. The black box marks the location of the area shown in (**b**). **b** Topography of the MVF (SRTM DEM). AVC, Ado'Ale volcanic complex. In red the magmatic segments and in green marginal volcanoes (triangles) and transverse structures (green shading) (Esri. "Hillshade" [Basemap]. "Terrain: Hillshade Gray". Apr 8, 2020. https://www.arcgis.com/home/item.html?id=d2f3e6dbfd7c457fa275dfb5a282523b)
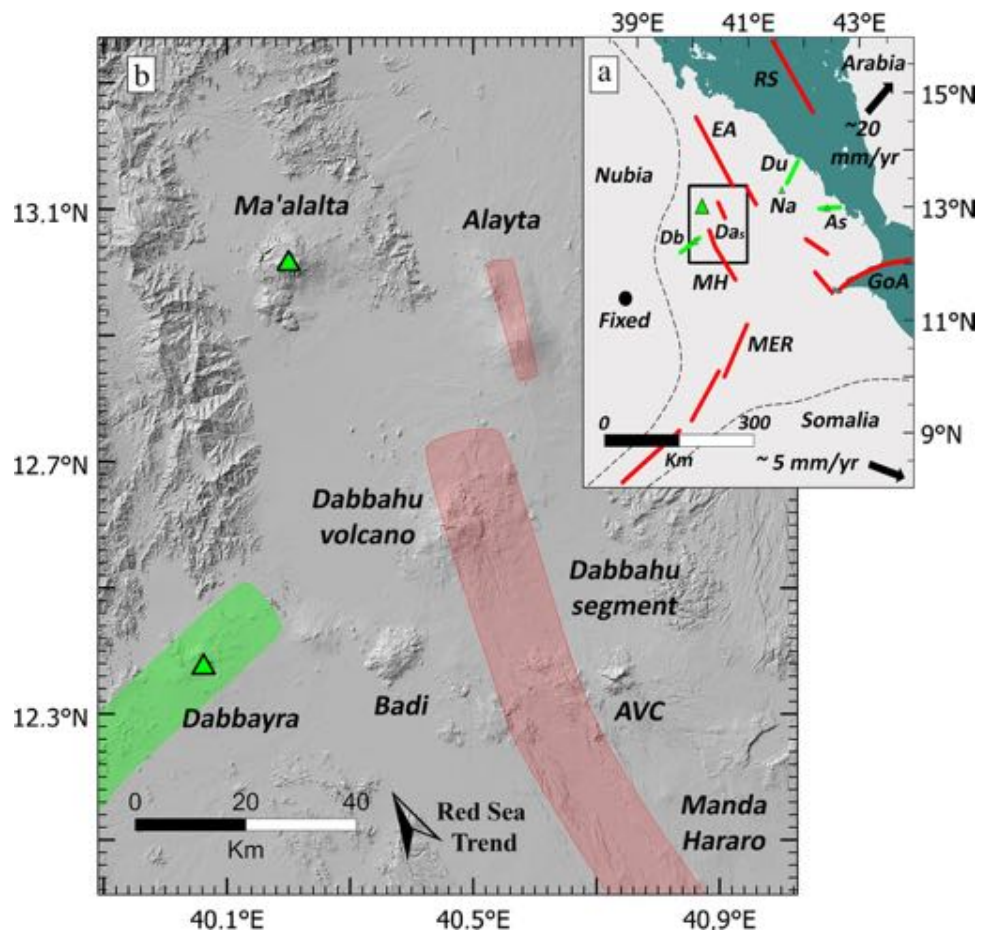
nearby magmatic segments is partial because of their remote location and because scientific interest has focused mainly on axial volcanism.

We provide new major and trace element analyses and the first pressure and temperature estimates of the MVF rock samples. The rocks were collected during the French-Italian campaigns in 1967–1973 (Varet 1978; Barberi et al. 1977; http://repositories.dst.unipi.it/index.php/afar-repositories). We integrated the volcanological, geochemical and petrological analyses with remote sensing-based mapping and local earthquake catalogues. We combined the diverse datasets in order to understand the characteristics of the MVF magmatic production, the relationship of the volcano with the other rift segments and the current magmatic and tectonic activity of Afar.

Geological background

The Afar depression

The Afar depression is a triple junction between the Red Sea, Gulf of Aden and Main Ethiopian Rifts, created by the divergent motions of the Nubian, Arabian and Somalian

plates. Afar is flanked by the Ethiopian Plateau to the west, by the Somalian Plateau to the south-east and the Danakil Block and Ali-Sabieh Block to the east. Initiation of volcanic activity in Ethiopia is thought to be caused by a mantle plume that produced the Ethiopian flood basalts (Marty and Gezahegn 1996; Pik et al. 1999; Kieffer et al. 2004) with the majority of the volume of basaltic magma erupted over only ~ 1 Myr at about 30 Ma (Zumbo et al. 1995; Hofmann et al. 1997). Starting from the Oligocene, magmatic activity occurred inside the newly forming Afar rift floor and progressively migrated towards the current magmatic segments through the Miocene (Wolfenden et al. 2005; Stab et al. 2016).

The Afar rift floor is mainly covered by the Stratoid Series (4–1 Ma), followed by the Gulf Basalt formation (1.1–0.6 Ma) (Barberi and Santacroce 1980; Kidane et al. 2003; Stab et al. 2016), while magmatism and extension are currently mainly localised to axial magmatic segments within the rift (Hayward and Ebinger, 1996; Wright et al. 2006; Fig. 1). In central and northern Afar, these magmatic segments (e.g. Dabbahu, Manda Hararo and Erta Ale) are oriented NNW-SSE, which is the orientation of the Red Sea (Fig. 1). The magmatic segments consist of fissural eruptions

associated with extensional fractures sometimes related to shield volcanoes (Oppenheimer and Francis 1998; Wright et al. 2006; Ferguson et al. 2010; Field et al. 2012, 2013; Medynski et al. 2015, 2016; Hagos et al. 2016). Volcanism close to the margins of the Afar floor is also reported. Barberi et al. (1970, 1974b) described transverse alignments of volcanoes (e.g. Dabbayra, Assab and Dubbi) situated both east and west of the magmatic segments in Afar (green segment in Fig. 1a) and oriented nearly orthogonally to the Red Sea trend. Furthermore, they also classified stratovolcanoes on either side of the rift, such as Nabro and Ma'Alalta, as marginal volcanoes (green triangles in Fig. 1a). These are large stratovolcanoes that produced caldera-forming explosive eruptions (Barberi et al. 1974a; Wiart and Oppenheimer 2005; Oppenheimer et al. 2019) and lava flows generally more alkaline with respect to the tholeiitic-transitional axial volcanism (Civetta et al. 1975; De Fino et al. 1978; Donovan et al. 2018). The most recent eruption of a marginal volcano was in 2011 at Nabro, which produced basaltic to basaltic trachyandesite tephra and lava (Hamlyn et al. 2018; Donovan et al. 2018). The MVF is located in the Northern sector of Afar, where the extension rate is ~20 mm/year in a ~NE-SW direction (Fig. 1) (McClusky et al. 2010).

The Ma'Alalta volcanic field

The MVF is surrounded by outcrops of Jurassic limestones and meta-sediment and meta-volcanic of the Neoproterozoic basement and is dominated by a 1745-m-high stratovolcano with nested calderas elongated NE-SW, approximately perpendicular to the Red Sea trend. The outer caldera is approximately 8×5 km, and the inner one is 5×2.5 km. At the base of the MVF sequence, Barberi et al. (1970) identified fissural basaltic lava flows, underlying three ignimbrite sheets alternated with pumice fall layers, and before the emplacement of the third ignimbrite unit, and basaltic scoriaceous deposits with associated small scoria cones. On top of this succession, they recognized obsidian flows, pyroclastic layers and porphyritic trachyte flows and domes that built the stratovolcano. The most recent products are felsic lava domes and obsidian flows, erupted along NNW-SSE fissures south of the stratovolcano. Barberi et al. (1974a) distinguished an earlier stratovolcano-building phase with felsic non-peralkaline lavas and a later phase that produced large-volume ignimbrites, intra-caldera domes and lava flows of peralkaline composition, particularly rich in sanidine phenocrysts (Barberi et al. 1970). The felsic domes and flows south of the stratovolcano are more peralkaline and silica-rich with respect to the stratovolcano products, and they are nearly aphyric (Barberi et al. 1970, 1974a). Wiart and Oppenheimer (2005) proposed a satellite-based map suggesting that the stratovolcano is flanked to the west and south-west by felsic domes and lava flows but also by recent mafic cinder cones and NNW-SSE fissural lava flows and to the east by more weathered and eroded lavas, named "Old Lava". K–Ar age determinations gave 0.55 ± 0.05 Ma for a lava sample at the base of the stratovolcano and 0.12 ± 0.05 Ma for a pantellerite obsidian south of the stratovolcano (Barberi et al. 1972).
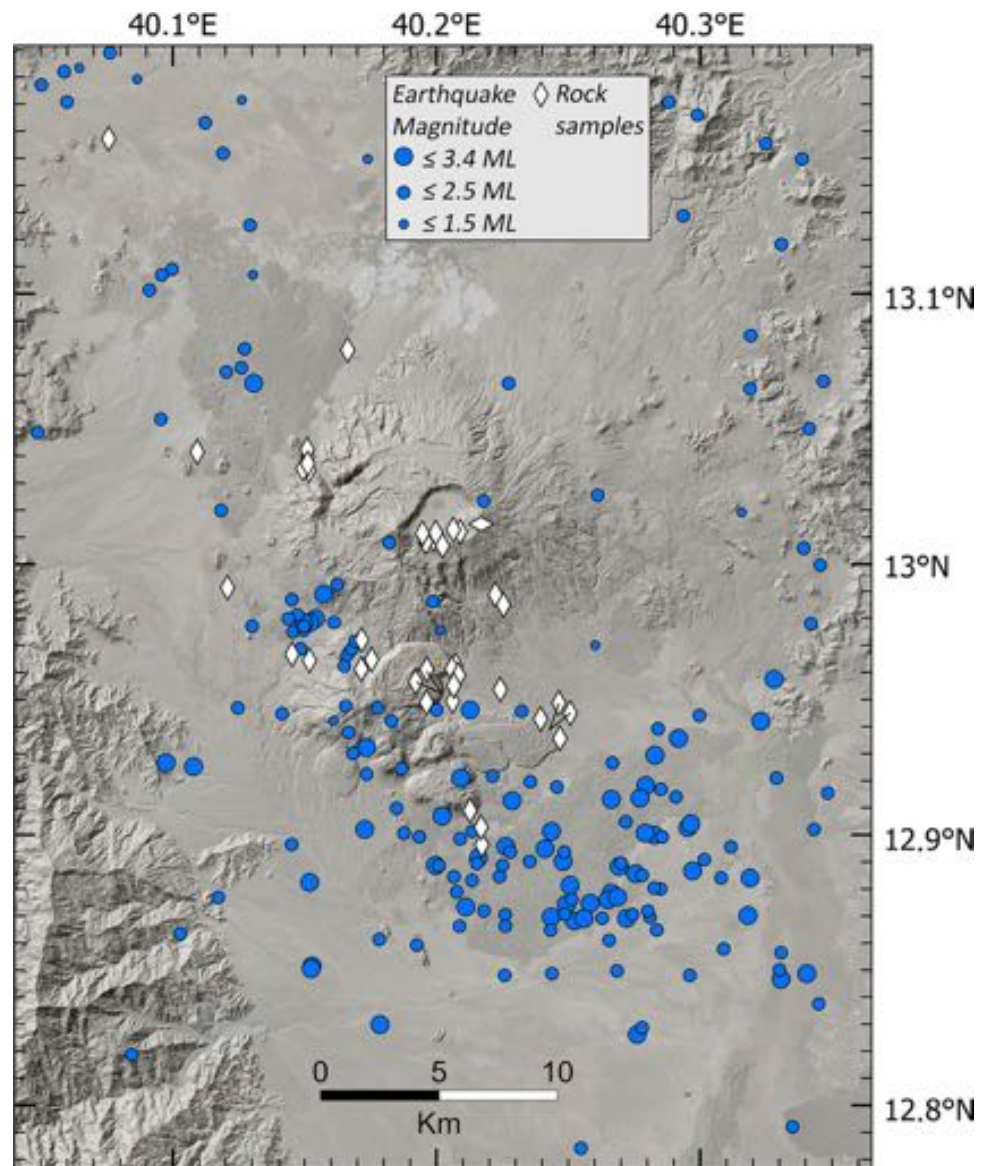
Methods

Rock samples and mapping

For this study, we used forty rock samples from the Afar Repository of the University of Pisa (http://repositories.dst.unipi.it/index.php/afar-repositories), collected between 1967 and 1973 in the MVF region (Fig. 2). The sampling sites have been identified using the original sampling map. The samples are mainly lavas with few pyroclastics (online resource Table 1) and cover the main phases of the MVF volcanic activity (Figs. 2 and 3). We examined the rock samples and thin sections and also investigated the spatial distribution of the erupted products using satellite images. We obtained a detailed map of the different lava flows of MVF by determining the type of erupted products through petrographic observations and reconstructing the spatial distribution of the products with Landsat satellite panchromatic images. We mapped all the volcanic and tectonic features, and by draping the satellite images onto the SRTM DEM (resolution of 1 arc-second), we interpreted the relative stratigraphy of the volcanic deposits. Based on the petrographic observations and the spatial distribution of the deposits, we selected lava samples for bulk rock and mineral chemical analysis.

Analytical methods for geochemistry and mineral chemistry

We selected 14 lava samples representative of the two phases of MVF and without signs of alteration in hand sample and thin section (Fig. 3; Table 1). All the samples were crushed and milled in agate jars and analysed for major elements by means of XRF using the spectrometer ARL 9400 XP of the University of Pisa. The Loss on Ignition (LOI) was determined at 950 °C. Three of these samples were previously analysed for major elements (Barberi et al. 1974a, b; Barberi et al. 1970; Tazieff et al. 1969) and are listed in online resource Table 2 but have not been inserted in the figures (the other literature data are present in both online resource Table 2 and figures). Trace element analysis was performed on 13 samples (Table 1) using inductively coupled plasma mass spectrometry (ICP-MS) with a PerkinElmer NexION 300X of the University of Pisa. About 50–60 mg of each powdered sample was dissolved in a mixture of HF and HNO_3 on a hot plate at ~170 °C in screw-top perfluoroalkoxy (PFA) vessel,

following the procedure used at the ICP-MS laboratory for igneous rocks. Ultrapure Milli-Q water was used for diluting the solution. A procedural blank and 3 references samples underwent the same procedure. The geochemical references materials used are RGM-1 (Rhyolite Glass Mountain) (Govindaraju 1994) and WS-E (Whin Sill Dolerite) (Govindaraju 1994) to verify the accuracy of the analysis and BE-N (alkali basalt) (Govindaraju 1980) to calibrate the equipment (Table 1). A solution containing ^{103}Rh, ^{187}Re and ^{209}Bi has been added to the unknown samples, blank and reference samples to be used as the internal standard.

Polished thin sections of five samples were studied by scanning electron microscopy (BSE imaging) and EDS microanalysis with the FEI Quanta 450 ESEM FEG provided with a QUANTAX XFlash Detector 6/10 at the University of Pisa. The mineral composition of five samples, one trachyte of the

first phase and one rhyolite and three basalts of the second phase (online resource Table 3), was analysed using the Electron Probe MicroAnalyzer (EPMA) 8200 Super Probe at the Department of Earth Sciences "Ardito Desio" of the University of Milan. Analytical conditions for minerals were 15 kV accelerating voltage, 5 nA beam current, 3 μm beam size and counting time of 20 s on peaks and 10 s in background.

Geothermobarometry

Four porphyritic samples, one trachyte of the first phase and three basalts of the second phase, were selected for mineral-melt geothermobarometry (Table 2; Fig. 3). The geothermobarometer of Masotta et al. (2013), based on the clinopyroxene-liquid equilibrium, was used for the stratovolcano trachyte. For the basalts, we used the cpx-liquid
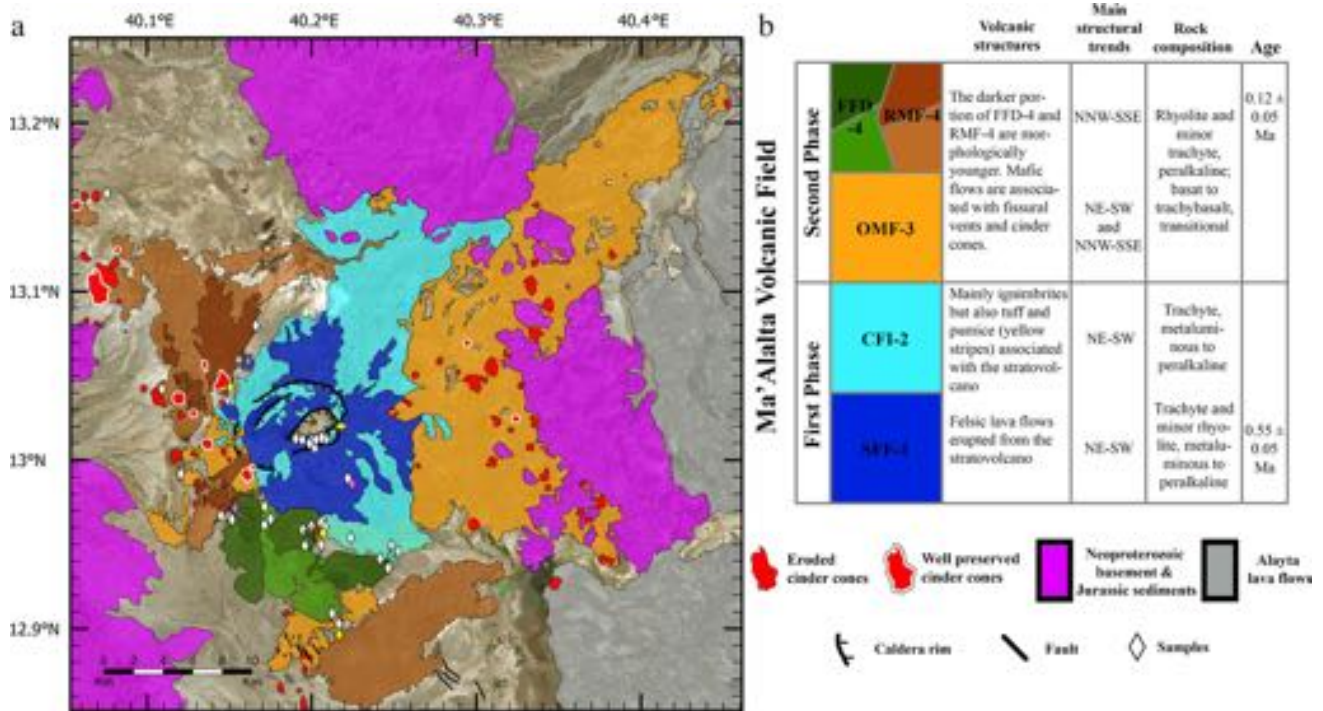
Fig. 3 a Geological map of the MVF, combining petrographic analysis, Landsat 5 satellite images, SRTM DEM and morphological observation. The horizontal diamond and World Imagery Source as in Fig. 2. The pink diamonds represent the literature dated samples (the one of FFD-4 is located in the original sampling map but not in the collection), while the yellow ones the samples used for the geothermobarometry estimates. **b** Stratigraphic column showing the main characteristics of the MVF deposits and their chronological order. SFF-1, stratovolcano felsic flows; CFI-2, calderas felsic ignimbrites; OMF-3, old mafic flows; RFM-4, recent mafic flows; FFD-4, felsic flows and domes. The numbers represent the reconstructed chronological order from the lower (1) to the higher (4) deposits (Ages from Barberi et al. (1972))

thermometer of Putirka (2008; Eq. 33) and the barometer of Neave and Putirka (2017). The feldspar-liquid and olivine-liquid equilibria of Putirka (2008; Eq. 22, 24a, 24b and 25a) were used for the stratovolcano trachyte and the basalts, respectively. For each sample, the whole rock analysis was used for the melt composition in equilibrium with the phenocrysts cores (Putirka 2008). The output pressure of the clinopyroxene-liquid geothermobarometers was used as input for the other geothermobarometers. Water concentrations from 1 wt% to 3 wt% were used in the modelling. Mineral-melt equilibrium was checked based on the distribution coefficient $KD_{(Fe-Mg)}^{cpx-liq} = 0.09\text{-}0.37$ for Masotta et al. (2013); $KD_{(Fe-Mg)}^{cpx-liq} = 0.27 \pm 0.03$ for Neave and Putirka (2017); $KD_{(Fe-Mg)}^{ol-liq} = 0.30 \pm 0.03$ for Putirka (2008); $KD_{(An-Ab)}^{pl-liq} = 0.10 \pm 0.05$ at T < 1050 °C and 0.27 ± 0.11 at T ≥ 1050 °C; and $KD_{(An-Ab)}^{afs-liq} = 0.27 \pm 0.18$ for Putirka (2008).

Seismicity

The seismological analysis was carried out using a combined dataset of local seismicity acquired during 2005–2013 in Afar (Fig. 2). The data were collected using consecutive local seismic networks during 2005–2006 (Ebinger et al. 2008), 2007–2009 (Belachew et al. 2011) and 2011–2013 (Illsley-Kemp et al. 2018). The latter seismic network was more sensitive to earthquakes in MVF, as the closest station was ~ 23 km from the stratovolcano, while the minimum distance was ~ 50 km during the earlier networks. We used the published earthquake catalogues from the above studies and isolated all the earthquakes that occurred near the MVF between longitude 39.90E–40.35E and latitude 12.70 N–13.20 N, giving a total of 229 events (Fig. 2), of which 34 were recorded between 2005 and 2006, 26 during 2007 and 2009 and 169 in 2011 and 2013.

Results

Geological map of MVF and relative chronology of the volcanic units

We identify two different phases of activity based on the relative chronology of the volcanic units, the petrographic analysis and the distribution of the erupted products in the satellite images (Fig. 3). The first phase started at 0.55 ± 0.05 Ma (Barberi et al. 1972) with the formation

Table 1 Major and trace element composition of MVF whole rocks

	First Phase					Second Phase								
	Stratovolcano felsic flows, SFF-1					Felsic flows and domes, FFD-4					Old and recent mafic flows, OMF-3 - RMF-4			
	Base		Top											
Sample	D 169	D 177	G33	K39	G28	G3	G10	G18	G14	G23	D170	G8	G16	G20
SiO$_2$ (wt%)	73.28	65.89	71.9	65.13	63.65	65.68	71.07	70.83	70.26	70.20	48.56	48.26	50.80	49.10
TiO$_2$	0.26	0.70	0.28	0.58	0.89	0.46	0.30	0.29	0.31	0.30	1.79	2.47	2.72	2.29
Al$_2$O$_3$	9.86	15.41	9.73	14.76	15.77	13.89	13.09	13.31	12.96	12.95	17.88	15.04	15.73	15.10
FeO$_{tot}$	6.00	3.48	5.84	5.15	5.26	5.35	3.78	3.93	3.56	3.67	8.53	9.52	11.42	9.59
MnO	0.21	0.07	0.21	0.20	0.18	0.24	0.12	0.13	0.11	0.12	0.14	0.16	0.19	0.17
MgO	0.21	0.69	0.21	0.37	0.55	0.23	0.12	0.18	0.11	0.13	7.21	7.77	4.69	7.25
CaO	0.40	1.93	0.39	1.55	1.95	1.59	0.51	0.69	0.52	0.52	11.33	10.67	8.27	10.89
Na$_2$O	5.15	4.72	5.01	5.79	5.63	6.02	5.60	5.64	5.59	5.94	2.71	2.61	3.74	2.80
K$_2$O	4.39	4.66	4.30	4.59	4.50	4.86	4.79	4.80	4.66	4.68	0.56	1.24	1.32	0.86
P$_2$O$_5$	0.05	0.18	0.04	0.16	0.29	0.08	0.05	0.05	0.05	0.05	0.32	0.39	0.49	0.43
L.O.I.	0.00	0.49	0.47	0.18	1.55	0.49	0.06	0.14	0.18	0.35	0.50	-	-	-
Sum	99.81	98.22	98.38	98.46	100.22	98.89	99.49	99.99	98.31	98.91	99.29	98.13	99.37	98.48
Mg#	5.83	25.97	5.98	11.29	15.61	7.07	5.32	7.50	5.18	5.90	59.93	59.09	42.10	57.23
Total Alkalis	9.54	9.38	9.31	10.38	10.13	10.88	10.39	10.44	10.25	10.62	3.03	3.85	5.06	3.66
A.I.	1.34	0.83	1.33	0.98	0.90	1.09	1.10	1.09	1.10	1.15	0.27	0.37	0.48	0.37
Peralkaline Rock type	P	-	P	-	-	C	C	C	C	C	-	-	-	-

	First Phase				Second Phase									Reference materials					
	Stratovolcano felsic flows, SFF-1				Felsic flows and domes, FFD-4					Old and recent mafic flows, OMF-3 - RMF-4									
Sample	K39[1]	G33[2]	G28[2]	D177[1]	G23[1]	G10[2]	G14[2]	G3[2]	G18[1]	G16[1]	G20[1]	D170[2]	G8[1]	RGM-1Ref[1]	RGM-1[1]	WSE Ref[1]	WSE[1]	WSE[2]	WSE Ref[2]
Li	26.8	54	18.1	23.7	27.9	16.9	17.7	18.4	19.1	10.0	6.3	4.1	5.4	61	64	13.5	15.0	13.7	13.5
Be	6.6	14.1	5.1	3.4	5.5	5.6	5.1	2.92	5.4	1.79	1.16	0.88	1.30	2.50	2.46	1.10	1.08	1.16	1.10
Sc	6.5	7.0	10.8	5.7	1.87	2.65	2.62	3.26	1.83	25.1	34	35	29.6	4.7	4.3	27.6	27.0	34	27.6
V	3.4	<3	14.4	34	<0.2	<3	<3	0.72	1.04	317	314	251	300	11.8	10.9	336	332	338	336
Cr	1.34	2.04	2.80	1.40	1.80	1.35	<1	<1	0.73	15.1	288	177	287	4.5	5.8	97	93	96	97
Co	0.98	0.10	2.77	5.3	0.27	0.18	0.03	0.15	<0.1	35	39	37	40	2.04	2.05	45	44	45	45
Ni	0.60	<0.7	1.94	2.96	0.29	<0.7	<0.7	0.79	0.29	17.6	81	69	103	3.4	4.0	54	55	56	54
Cu	7.1	<11	12.1	12.7	21.6	<11	<11	11.9	<3	42	79	47	63	11.1	10.0	66	62	56	66
Zn	152	306	132	56	163	130	131	105	135	118	116	68	93	33	30.2	113	112	112	113
Ga	29.8	37	25.3	20.5	31.0	29.6	29.2	28.7	30.4	20.1	16.7	16.4	18.1	16.1	15.4	21.6	20.8	21.4	21.6
Rb	126	261	108	126	126	125	124	79	109	32.9	21.4	12.8	29.1	150	146	25.8	25.0	17.9	25.8
Sr	79	<12	232	109	<4	<12	<12	<12	8.4	327	365	402	463	105	131	407	394	391	407
Y	77	196	67	30.8	80	80	81	53	83	38	26.2	20.9	25.0	23.5	23.3	31.8	31.7	29.6	31.8
Zr	791	2070	657	289	734	738	745	457	697	223	155	115	179	228	223	204	203	210	204
Nb	152	371	122	65	130	132	136	96	130	44	36	25.8	41	9.1	8.8	17.9	17.6	18.3	17.9
Mo	3.5	3.5	2.29	2.62	7.0	4.7	4.9	2.14	1.88	2.04	1.56	1.01	1.81	2.44	2.48	3.5	3.4	3.4	3.5
Cs	0.85	1.46	<1	0.72	1.32	1.50	1.42	<1	0.42	0.38	0.22	<1	0.25	10.1	10.4	0.47	0.46	0.27	0.47
Ba	691	26.9	1065	567	4.7	10.9	<6	44	17.5	345	317	207	386	827	871	335	348	347	335
La	99	260	86	56	105	109	110	70	99	33	25.1	19.2	27.8	22.9	23.8	26.6	26.8	27.3	26.6
Ce	210	526	182	111	223	231	234	152	209	69	53	41	59	46	47	60	59	62	60
Pr	23.3	57	19.8	12.3	24.9	25.3	25.5	17.1	23.4	8.5	6.6	5.1	7.4	5.3	5.4	7.7	7.8	8.0	7.7
Nd	85	202	73	43	92	94	93	65	88	34	26.6	21.0	29.6	19.2	19.5	32.8	33	34	32.8
Sm	16.1	38	13.7	8.0	17.5	17.5	17.5	12.3	17.2	7.5	5.7	4.4	6.1	4.0	4.0	8.8	8.8	9.1	8.8
Eu	2.94	2.80	3.16	1.30	1.14	1.14	1.12	1.60	1.28	2.33	1.93	1.58	2.02	0.62	0.62	2.20	2.24	2.25	2.20
Gd	13.4	34	12.2	6.7	14.9	15.5	15.8	10.9	15.0	7.2	5.3	4.6	5.6	3.7	3.6	7.2	7.2	7.3	7.2
Tb	2.20	5.7	2.01	1.07	2.45	2.55	2.58	1.73	2.43	1.16	0.84	0.70	0.84	0.60	0.61	1.08	1.10	1.11	1.08
Dy	13.5	35	12.0	6.0	14.5	15.3	15.3	10.0	14.8	6.8	4.8	4.0	4.7	3.7	3.8	6.1	6.3	6.3	6.1
Ho	2.75	7.1	2.43	1.20	2.95	3.04	3.03	1.98	2.94	1.34	0.95	0.78	0.90	0.76	0.79	1.18	1.18	1.17	1.18

Note: C, Comendite; P, Pantellerite; L.O.I., Loss Of Ignition; A.I., Agpaitic index. Total iron as FeO, Eu* = (SmN + GdN)/2, na = not analyzed. [1] first batch of analysis and relative reference materials; [2] second batch of analysis and relative reference materials

Table 2 Pressure and temperature conditions of crystallization from mineral geothermobarometers: K39, SFF-1:D170, G20, G8, OMF-3-RMF-4

Sample	Clinopyroxene			Plagioclase				K feldspar			Olivine		
	H_2O input			P input	H_2O input			P input	H_2O input		P input	H_2O input	
K39		P_1	T_1			P_2	T_2			T_2			
	1%	1.34	925	1.5 Kbar	1%	2.7	954	1.5 Kbar	1%	857			
	2%	1.41	919	1.5 Kbar	2%	2.1	928	1.5 Kbar	2%	857			
	3%	1.49	914	1.5 Kbar	3%	1.7	902	1.5 Kbar	3%	857			
	n°	15	15		n°	3	3		n°	5			
	SEE	±1.15 kbar	±24 °C		SEE	±3.8 kbar	±36 °C		SEE	±23 °C			
G20	H_2O input	P_3	T_2	P input	H_2O input	P_2	T_2				P input	H_2O input	T_2
	1%	4.1	1176	4 Kbar	1%	4.0	1162				4 Kbar	1%	1178
	2%	3.9	1161	4 Kbar	2%	2.5	1125				4 Kbar	2%	1159
	3%	3.8	1146	4 Kbar	3%	1.1	1091				4 Kbar	3%	1140
	n°	11	11		n°	2	2					n°	2
	SEE	±1.4 kbar	±45 °C		SEE	±3.8 kbar	±36 °C					SEE	±43 °C
D170	H_2O input	P_3	T_2	P input	H_2O input	P_2	T_2				P input	H_2O input	T_2
	1%	6.6	1193	6.5 Kbar	1%	7.8	1210				6.5 Kbar	1%	1184
	2%	6.5	1177	6.5 Kbar	2%	6.2	1171				6.5 Kbar	2%	1165
	3%	6.3	1161	6.5 Kbar	3%	4.7	1134				6.5 Kbar	3%	1147
	n°	7	7		n°	7	7					n°	4
	SEE	±1.4 kbar	±45 °C		SEE	±3.8 kbar	±36 °C					SEE	±43 °C
G8	H_2O input	P_3	T_2										
	1%	2.8	1155										
	2%	2.6	1140										
	3%	2.5	1125										
	n°	5	5										
	SEE	±1.4 kbar	±45 °C										

n° number of analysed samples, *SSE* error sum of squares. Subscript indicates the reference work for the geothermobarometric calculation: *1* Masotta et al.(2013), *2* Putirka (2008), *3* Neave and Putirka (2017)

of the stratovolcano and was later affected by a caldera-forming stage, producing trachytic-rhyolitic lava flows and ignimbrites (Fig. 3, online resource Fig. 1). This activity was followed by the second phase (0.12 ± 0.05 Ma, Barberi et al. 1972) producing multi-vent mafic and felsic eruptions. This phase produced a NNW-SSE-trend of fissural basaltic-trachybasaltic lava flows and cinder cones and rhyolitic-trachytic lavas and domes (Fig. 3, online resource Fig. 1).

The stratovolcano and caldera-forming phase (first phase)

Based on the available samples of the first phase, two stages can be distinguished: a mainly effusive stage, consisting of metaluminous to peralkaline trachytic-rhyolitic rocks building the central edifice, called the stratovolcano felsic flows (SFF-1), and a caldera-forming stage, consisting of metaluminous to peralkaline trachytic pyroclastic flow deposits, called calderas felsic ignimbrites (CFI-2) which include the final silicic activity of the calderas (Fig. 3; Table 1; online resource Table 1). We observed an upward variation in size, type and abundance of phenocrysts from the base to the top of the stratovolcano felsic lava flows. The seven samples from the top have up to 40 vol% of phenocrysts consisting of alkali feldspar reaching 1 cm in size and minor plagioclase, fayalite, slightly pleochroic clinopyroxene and, in one sample, arfvedsonite (Fig. 4; online resource Fig. 2a; online resource Table 1). Plagioclase is mainly andesine and minor oligoclase ($Ab_{51-68}An_{26-47}$); alkali feldspar is mainly anorthoclase ($Ab_{63-72}Or_{15-36}$); clinopyroxene is augite ($Wo_{38-44} Fs_{23-57}$) (online resource Fig. 3a; online resource Table 3). Apatite and Fe-Ti oxides are the main accessory phases. The groundmass is holocrystalline or nearly so, and it is composed of the same crystals as the phenocrysts except for fayalite. Two samples from the top rim of the inner caldera display phenocrysts of quartz in addition to alkali feldspar and minor pleochroic clinopyroxene, arfvedsonite and aenigmatite (online resource Fig. 2b; online resource Table 1). The three samples from the base of the stratovolcano have lower phenocryst abundance (up to 20 vol%) and smaller phenocryst in size compared to samples from the top (Fig. 4; online resource Fig. 2c; online resource Table 1). Also, no minerals indicative of peralkalinity are observed.

The multi-vent mafic and felsic phase (second phase)

During the second phase, fissural eruptions occurred along a ~ 35-km-long NNW-SSE trending zone. We identified three groups of products—old mafic lava flows (OMF-3), felsic lava flows and domes (FFD-4) and recent mafic lava flows (RMF-4)—erupted by fissural vents with numerous cinder cones forming monogenetic and polygenetic small volume volcanic edifices distributed along the NNW-SSE trending zone (Fig. 3).

The FFD-4 mainly occur south-west of the stratovolcano (Fig. 3). The samples are comendite rhyolite and minor trachyte lavas, scarcely porphyritic or aphyric (online resource Fig. 1; Table 1; online resource Table 1). Sanidine and clinopyroxene (hedenbergite $Wo_{43-46}Fs_{51-55}$; online resource Fig. 3b; online resource Table 3) are the main phenocrysts but fayalite, aenigmatite and arfvedsonite can be found in some samples (Fig. 4; online resource Fig. 4; online resource Table 1). The groundmass varies from holocrystalline to hypohyaline, and it is dominated by alkali feldspar, clinopyroxene and Fe-Ti oxides with sporadic fayalite, apatite and plagioclase.

The OMF-3 and RMF-4 groups (Fig. 3) are basalt and trachybasalt lava flows and cinder cones (online resource Fig. 1; Table 1; online resource Table 1) that differ in their morphological features and degree of weathering (Fig. 5a,b). The majority of OMF-3 lavas and poorly preserved cinder cones (Fig. 5a) are east of the volcano, while the RMF-4, associated to relatively well-preserved cinder cones (Fig. 5b), are located along the northern sector of the NNW-SSE trending zone and at its southern tip. All the mafic products show olivine, clinopyroxene and plagioclase phenocrysts, with large variations in their relative abundance (Fig. 4; online resource Fig. 5; online resource Table 1). The groundmass is from hypohyaline to hypocrystalline, with clinopyroxene, plagioclase and opaques. In the mafic samples, plagioclase is labradorite to bytownite ($Ab_{17-44}An_{54-82}$), olivine is Fo_{77-84} (the tephroite component is $Tp_{0.4-0.2}$), and clinopyroxene is augite with minor diopside ($Wo_{39-45}Fs_{9-16}$) (online resource Table 3; online resource Fig. 3c). Presence of reversed zoning in clinopyroxene, plagioclase and olivine crystals has been observed. In one case (sample G8), the large variation of clinopyroxene core composition in the augite field towards the hedenbergite endmember ($Wo_{41-48}Fs_{9-32}$) compared to the more homogeneous rims ($Wo_{43-47}Fs_{9-13}$) indicates mixing processes with evolved and peralkaline lavas. Sample D170 shows common reverse zoning in olivine, again an evidence of mixing of magmas with different degrees of chemical evolution.

Relative chronology of the volcanic units

The oldest products of MVF are the SFF-1, dated at 0.55 ± 0.05 Ma (Barberi et al. 1972), followed by the CFI-2 (Fig. 3b). We can identify at least two major explosive events that produced ignimbrite deposits, based on the presence of two calderas.

Our interpretation of the relationship between the first phase and the OMF-3 differs from Wiart and Oppenheimer (2005). We suggest that the neat and relatively straight

Fig. 4 Transmitted light petrographic images of MVF representative samples. **a** G28, stratovolcano felsic flows top; **b** D177, stratovolcano felsic flows bottom; **c** G23, felsic flows and domes; **d** K35, recent mafic flows. Cpx, clinopyroxene; Afs, alkali feldspar; Pl, plagioclase; Ol, olivine. Location and petrographic details of the samples are in online resource Table 1

4.8 mm
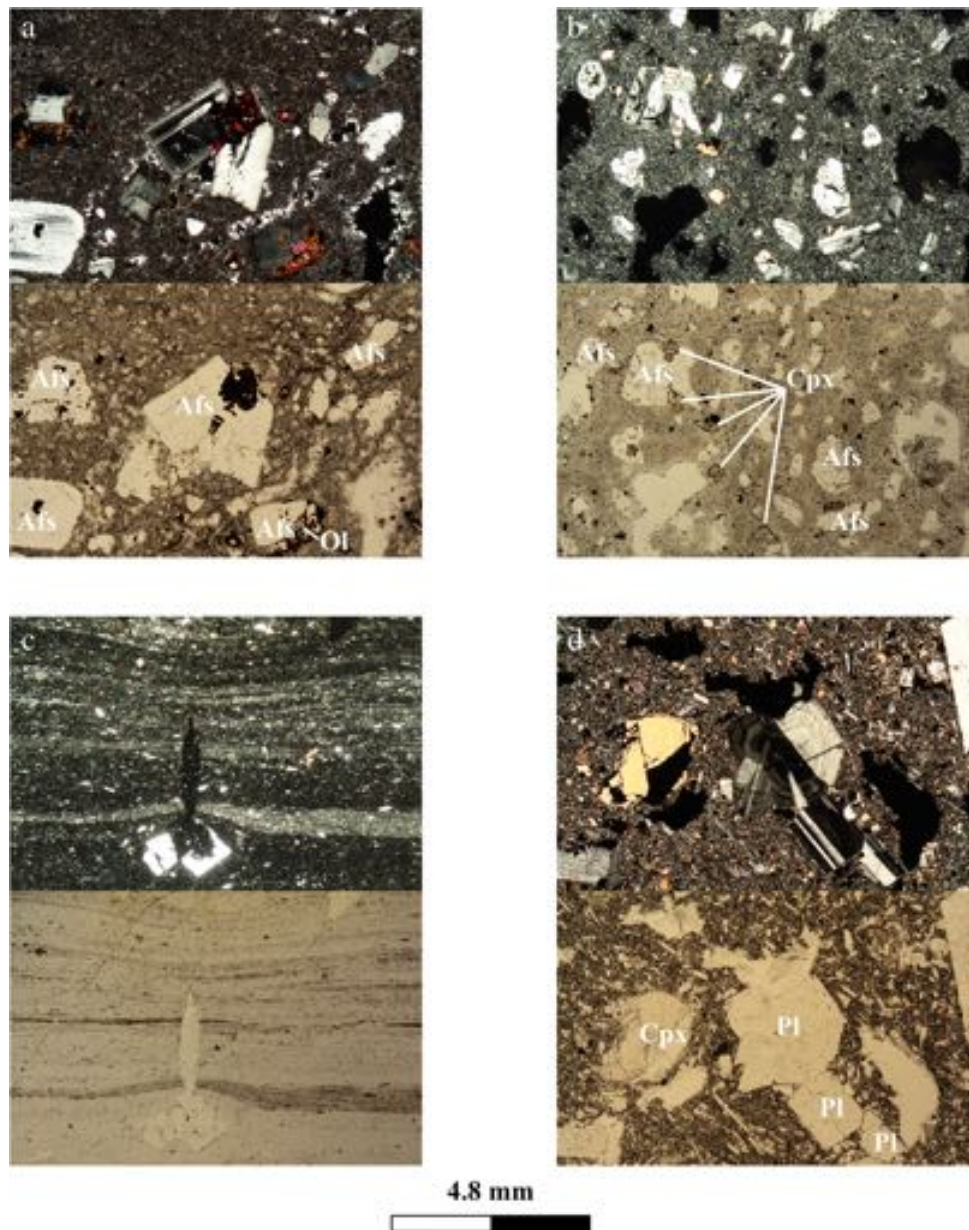
contact (N-S) on the eastern side of the stratovolcano (Fig. 5c) and the outcropping of the OMF-3 products on the western flank of the stratovolcano (online resource Fig. 6) indicate that they post-date the stratovolcano. Otherwise, the pyroclastic flows responsible for the ignimbrites would be easily emplaced on the OMF-3 east of the stratovolcano due to their proximity to the edifice and the absence of a topographic boundary. This would lead to an irregular contact due to the overlapping of the ignimbrites and a fan-like geometry of the felsic flows (instead of an abrupt stop at the contact with the OMF-3; Fig. 5c; online resource Fig. 6). Regarding the western flank of the stratovolcano, it is unlikely that the OMF-3, if emplaced before it, would result in topographic continuity (similar slope and altitude;

online resource Fig. 6) with the edifice and not covered by the stratovolcano products. Moreover, an outcropping portion of the ignimbrite deposit on the eastern flank of the stratovolcano is completely surrounded by OMF-3 mafic lava flows. These last observations indicate that the products of the first phase were deposited before the OMF-3. Based on the degree of erosion of lava flows and cinder cones, we classify OMF-3 as older than RMF-4 (Fig. 5a,b; online resource Fig. 6). The FFD-4 south of the stratovolcano is dated by Barberi et al. (1972) at 0.12 ± 0.05 Ma. At the small scale, the well-preserved fan-like geometry of the northernmost lava flow of FFD-4 (preserved also in the portion where FFD-4 and RMF-4 are not in contact) indicates that FFD-4 precedes RMF-4 but, at the same time, the undulated
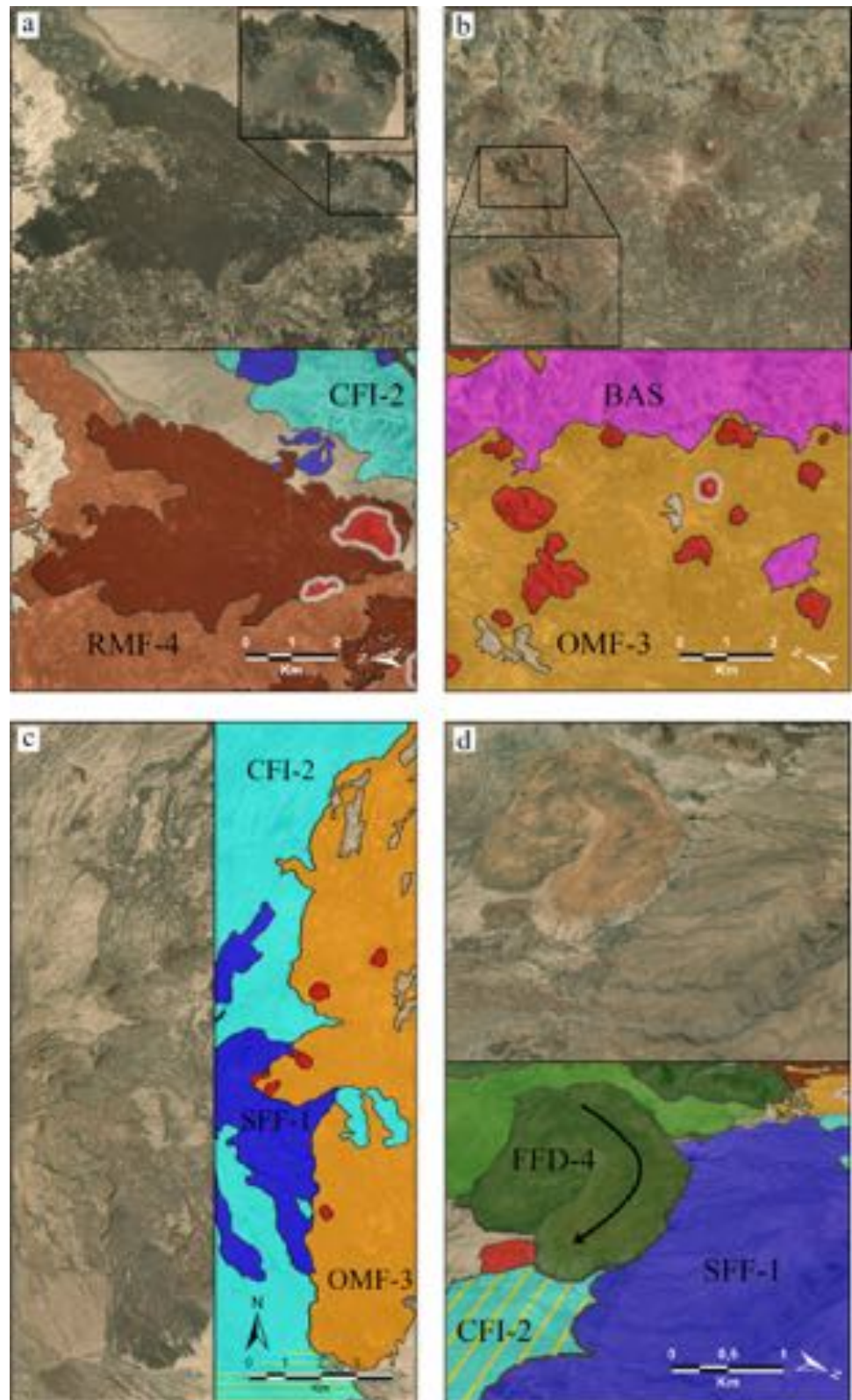
front at the contact with the basalts (online resource Fig. 6) would suggest the opposite. Due to these uncertain observations of the only contact between RMF-4 and FFD-4 and

the heterogeneous colour and surface morphology of both RMF-4 and FFD-4 (darker and lighter portions in Fig. 3), we suggest that they were likely emplaced during roughly the

same time period. Despite the lack of certainty about their age relationship, as a whole, they are the youngest products of the MVF eruptive history as they are emplaced after the stratovolcano activity, which also influences the flow directions of the upper products (Fig. 5d, online resource Fig. 6).

Major and trace element geochemistry

In the total-alkali vs silica diagram (TAS; online resource Fig. 1), the analysed MVF rocks fall in the basalt, trachybasalt, trachyte and rhyolite fields and define a compositional gap (Daly Gap), from 51 to 64 wt% SiO_2.

The SFF-1 rocks are mainly trachytes with few rhyolites (online resource Fig. 1). The samples from the top of the edifice are prevalently peralkaline (comenditic trachyte and pantellerite), while the rocks at the base are metaluminous trachytes, although very close to peralkalinity, and a pantellerite (Table 1; online resource Table 2). The variable degree of chemical evolution of the samples defines a differentiation trend of decreasing Al_2O_3, CaO, TiO_2 and P_2O_5, corresponding to fractionation of feldspar, pyroxene, Ti-Fe oxides and apatite, with nearly constant alkalies, while FeO_t increases in the most evolved rhyolitic samples (Fig. 6a). Accordingly, the elements Ba, Sr and Eu, strongly compatible in feldspars, reach the maximum depletion in the most evolved sample (Figs. 6b and 7).

The FFD-4 products are prevalently rhyolitic (online resource Fig. 1) and are more silica- and alkali-rich and more peralkaline (comendite and comenditic trachyte) with respect to the SFF-1 samples taken as a whole (Table 1; Fig. 6; online resource Table 2). The trace element patterns of FFD-4 samples are similar to each other and have greater negative anomalies in Sr, Eu, Ba, Ti and P compared to the stratovolcano (Fig. 7), which may indicate a higher degree of differentiation by fractionation of feldspar, Ti-Fe oxides and apatite. The G3 comenditic trachyte (the least evolved sample of the FFD-4) is the least enriched in REE and has the smallest negative Eu and Ba anomalies (Fig. 7) and shows the same ratios of highly incompatible elements (e.g. Zr/Nb; online resource Fig. 8).

The OMF-3 and RMF-4 products are basalts and trachybasalts (online resource Fig. 1; Table 1; online resource Table 2). All the samples have relatively low Mg# (< 60) and are all olivine-hypersthene normative (online resource Table 4). They all have no Eu anomalies (Fig. 7). Fractionation of olivine, clinopyroxene and Cr-spinel is active in the mafic reservoirs, as shown by the range in MgO and CaO (Fig. 6a) and Ni and Cr (online resource Fig. 7).

Overall, the whole distribution of the compatible elements indicates differentiation by crystal fractionation of olivine, pyroxene, feldspar, Cr-spinel, Ti-Fe oxides and apatite starting from transitional basalts, as already proposed for Dabbahu volcano (Barberi et al. 1975; Field et al.

2013; Fig. 6a; online resource Fig. 7). The distribution of the incompatible elements is also similar to the Dabbahu volcano samples (online resource Fig. 7, 8; Hutchison et al. 2018) with the exception of Y and Zr, slightly depleted in the MVF products for the same Th content. Moreover, the distribution of the MVF incompatible elements (Nb, Zr, Ta, Y, Vs and Th in online resource Figs. 7 and 8) shows good positive correlations going through zero (e.g. Th/Rb = 0.12 ± 0.02, Nb/Zr = 0.20 ± 0.02) suggesting a genetic link between mafic and the whole felsic products. Due to the small dataset and to the presence of the Daly Gap, it is however difficult to give a certain interpretation regarding the correlation between mafic and felsic products.

The comparison between the felsic rocks of SFF-1 and FFD-4 indicates different extent of fractional crystallization of feldspar, as suggested by the negative anomalies of Eu, Sr and Ba and of apatite and Ti-oxide as indicated by the negative anomaly of P and Ti, respectively (Fig. 7). Moreover, the Sr and Ba are remarkably lower in FFD-4 for the same Th (or Nb and Zr) content with respect to SFF-1 (Fig. 6b). Since accumulation of feldspar in SFF-1 can be excluded because it is not confirmed by Al_2O_3 vs. SiO_2 (Table 1; Fig. 6a), a major fractionation of feldspar for FFD-4 at the same evolution degree of SFF-1 is hypothesized. The trace element differences indicate that the two felsic rock suites were originated by different differentiation paths.

Geothermobarometry

Our geothermobarometric calculations (Table 2) based on clinopyroxene of the SFF-1 trachyte indicate crystallization pressures on the order of $1.34–1.49 \pm 1.15$ kbar. The crystallization temperature was $914–925 \pm 24$ °C for clinopyroxene, $902–954 \pm 36$ °C for plagioclase and 857 ± 23 °C for alkali feldspar. A higher crystallization pressure is obtained for the RMF-4 mafic magma of the lava flow south of the stratovolcano ($3.8–4.1 \pm 1.4$ kbar for clinopyroxene and $1.1–4.0 \pm 3.8$ kbar for plagioclase). The crystallization temperature was $1146–1176 \pm 45$ °C for clinopyroxene, $1091–1162 \pm 36$ °C for plagioclase and $1140–1178 \pm 43$ °C for olivine (only two analyses). The crystallization pressure obtained for the RMF-4 mafic magma of the lava flow north-west of the stratovolcano is still higher, $6.3–6.6 \pm 1.4$ kbar for clinopyroxene and $4.7–7.8 \pm 3.8$ kbar for plagioclase. The crystallization temperature was $1161–1193 \pm 45$ °C for clinopyroxene, $1134–1210 \pm 36$ °C for plagioclase and $1147–1184 \pm 43$ °C for olivine. Finally, the crystallization pressure obtained for the RMF-4 magma associated to a scoria cone in close proximity to the FFD-4 felsic centres, just south of the stratovolcano, is $2.5–2.8 \pm 1.4$ kbar. This estimation came from analysis of one clinopyroxene core and four rims which were found in equilibrium with melt. This is supported by ten analyses of rims close to the equilibrium range ($KD_{(Fe–Mg)}^{cpx−liq} = 0.31$

Fig. 6 a Major element Harker diagrams. The Dabbahu volcano whole rocks analyses are from Field et al. 2013 and Barberi et al. 1975. **b** Ba and Sr trace element diagrams. The Dabbahu volcano whole rocks analyses are from Hutchison et al. (2018). SFF-1, stratovolcano felsic flows; FFD-4, felsic flows and domes; RMF-4-OMF-3, recent-old mafic flows
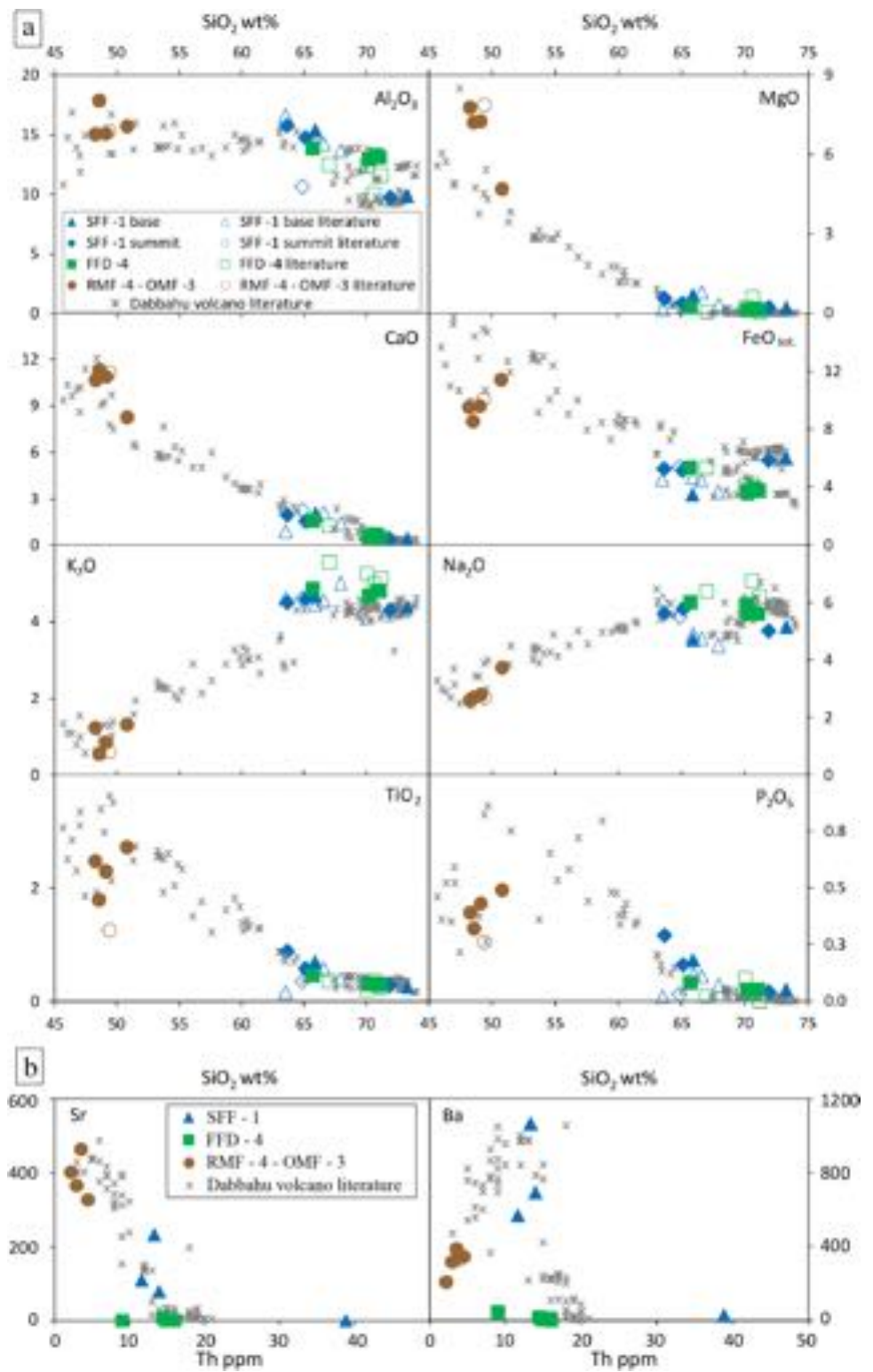

and 0.32) giving crystallization pressures of 2.4–2.7 ± 1.4 kbar. The crystallization temperature for core and rim analyses in equilibrium is 1125–1155 ± 45 °C.

We then derived the corresponding depths assuming a 270 bar/km geobaric gradient (Best 2013) and using

clinopyroxene results because of the lower errors. The obtained crystallization pressures correspond to a5-km depth for the SFF-1 trachyte and to 9–10-km, 14–15-km and 23–24 km depths for the mafic products.

Fig. 7 Chondrite-normalized REE patterns and primitive mantle-normalized trace element spider diagrams. SFF-1, stratovolcano felsic flows; FFD-4, felsic flows and domes; RMF-4-OMF-3, recent-old mafic flows. Normalizing values after McDonough and Sun (1995)
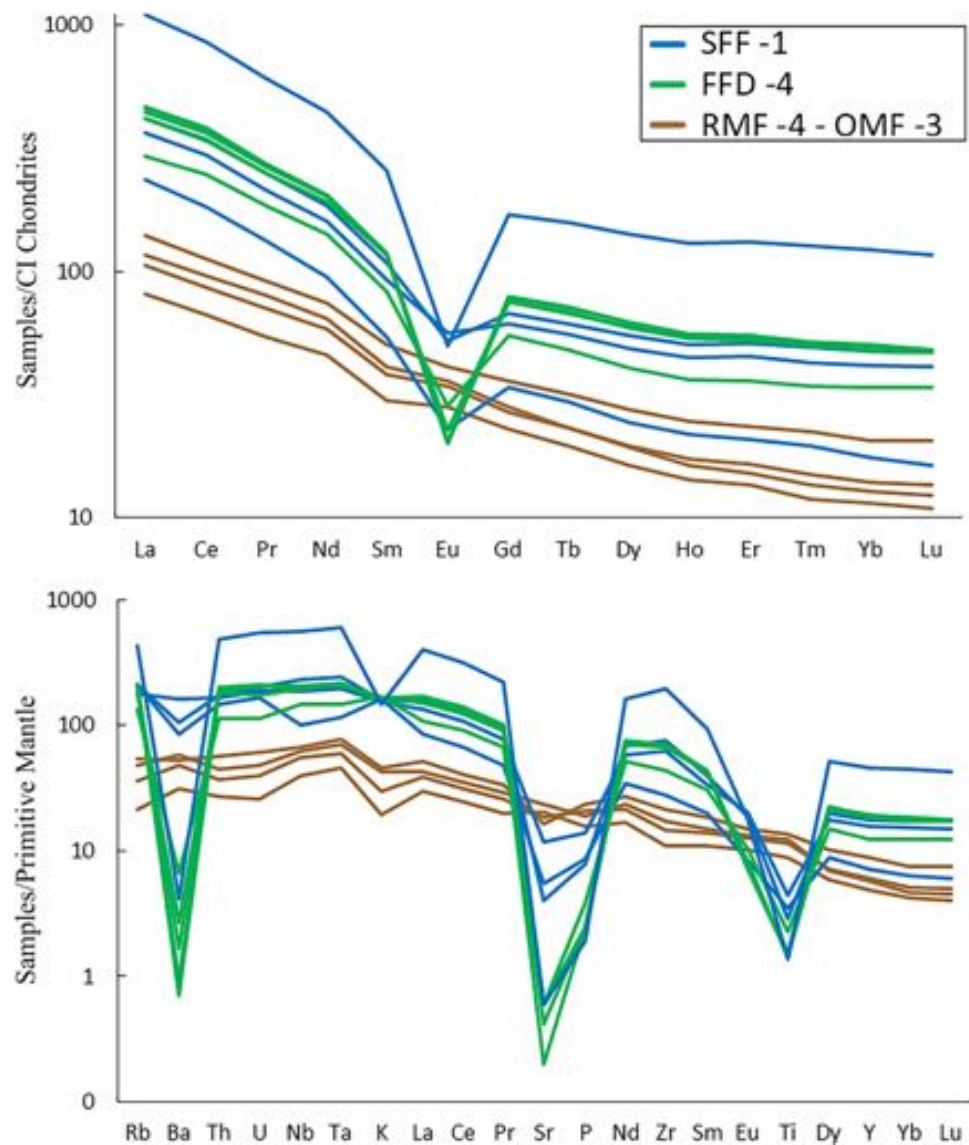
Structures and seismicity

En-echelon faults which are ~2-km long strike roughly parallel to the Red Sea trend and are clearly visible in the younger units at the southern tip of the MVF, and another NE-SW trend is defined by the elongation of the MVF calderas (Fig. 8). Furthermore, the distribution, morphology and elongation direction of the cinder cones are consistent with the two main trends (Fig. 8; Table 3). We identified three different groups of cinder cones based on their spatial distribution, and when the cone shapes were preserved, we also measured the direction of cone alignment using at least 3 cones closer than 400 m from each other, and the elongation direction using cones with aspect ratio > 1.4. The largest group of cinder cones is along the NNW-SSE trending zone west of the stratovolcano with up to 70 cones distributed along a zone striking 332° N, roughly parallel to the Red Sea

trend. Also, the alignment of the cones within this group has a trend varying between 327° E and 351° E, and the cones show predominant elongation varying from 321° E to 17° E, both subparallel to the Red Sea trend (Fig. 8). Altogether, the products of the second phase west of the stratovolcano occur over a ~35-km-long, NNW-SSE trend. East of the stratovolcano, two smaller groups of cones have been identified associated only with the OMF-3. A group of 19 cones show a trend of 317° N, similar to the western cones, while the remaining 26 cones are aligned 49° N, parallel to the elongation direction of the calderas. Most of the cones east of the calderas are not elongated nor aligned (Fig. 8).

The majority of the seismicity in MVF occurs along a ~35-km-long, NNW-SSE trending region with the alignment of earthquakes corresponding to the largest group of cinder cones and to the recent flows (FFD-4 and RMF-4) (Fig. 8). The magnitude varies between 1.06 and 3.37 and
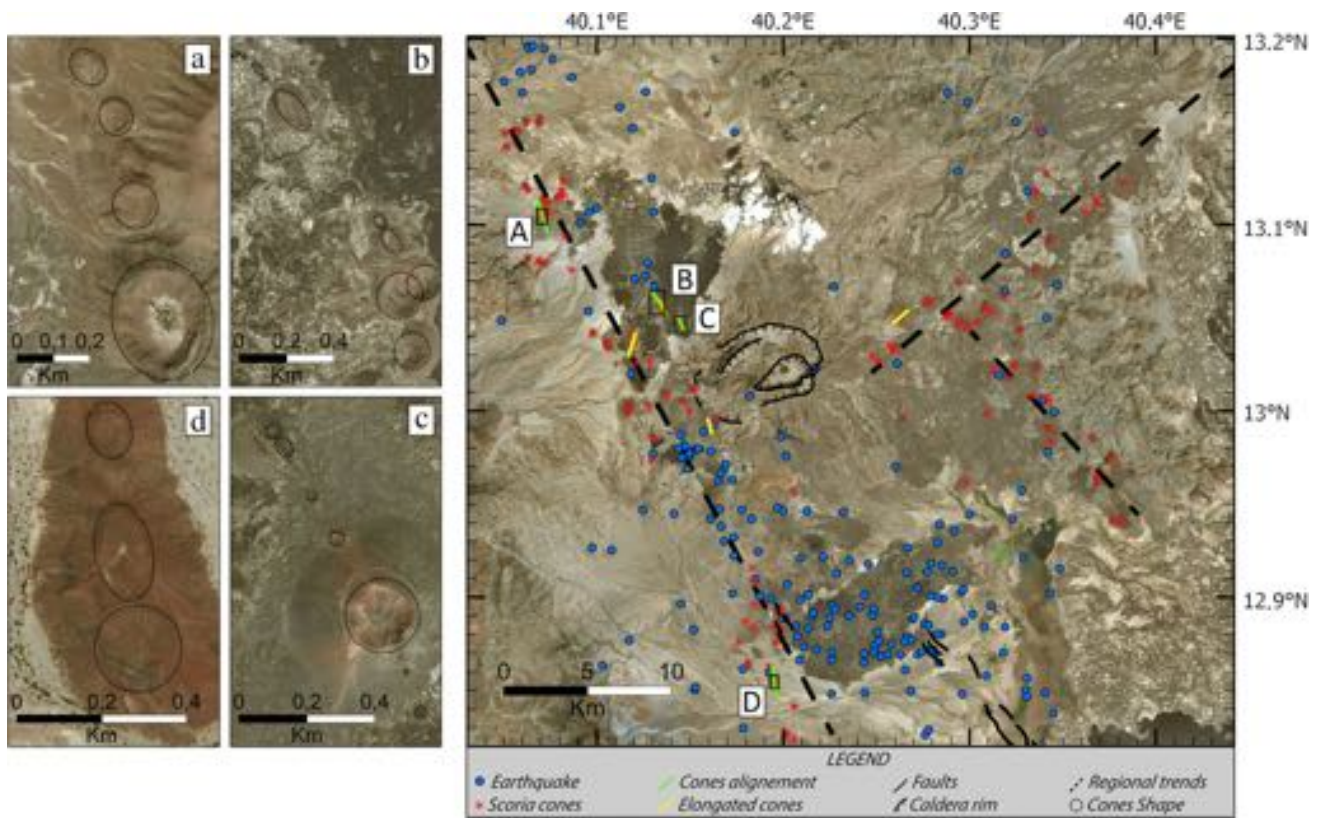
Fig. 8 Distribution of earthquakes (blue dots), cinder cones (red asterisks) and faults (solid black lines) of the MVF. **a-d** Elongated (351° E, 347° E, 17° E, 336° E and 321° E) and aligned (343° E, 327° E, 331° E and 351° E) cones (black dotted line). World Imagery Source as in Fig. 2

gives a mean of 2.22. Most earthquakes in the alignment are observed at the southern end with good correlation to where the most recent RMF-4 was erupted and where faults cutting these flows and surficial sediments occur. A smaller group of earthquakes is located in eastern parts of the MVF in the area between the OMF-3 and the basement, indicating that this region is not the main locus of seismicity at present. No significant seismicity occurs at the MVF calderas.

Discussion

Evolution of the MVF: from caldera activity to rift segment development

Two main phases of activity were identified during the evolution of MVF, based on the integration of volcanological, geochemical, petrological, structural and seismological evidence.

The first phase began at 0.55 Ma (Barberi et al. 1972) with explosive and effusive activity from a central vent

Table 3 Spatial distribution and elongation of the cinder cones

	Main trend		Alignment		Elongation	
	Degree	N° of cones	Degree	N° of cones	Degree	Aspect ratio
NNW-SSE distribution of cones west of the stratovolcano	332° N	70	351° N	3	351° N	1.5
			327° N	6	347° N	1.4
			331° N	2 + pit craters	17° N	1.4
			343° N	4	336° N	1.55
					321° N	1.5
NNW-SSE distribution of cones east of the stratovolcano	317° N	19				
NE-SW distribution of cones east of the stratovolcano	49° N	26			49° N	1.65

that built the stratovolcano. The two caldera structures suggest that the volcano was fed by a shallow crustal magma chamber, at ~ 5-km depth according to geobarometry applied to the lavas of the stratovolcano summit. This phase is dominated by structures trending NE-SW as indicated by the caldera elongation. Furthermore, this trend has been observed also in the NE-SW alignment of OMF-3 cinder cones east of the stratovolcano. This cinder cone alignment suggests that a tectonic structure orthogonal to the current rift axis (transverse alignment) existed during the formation of the stratovolcano and controlled the emplacement of the OMF-3 cinder cones aligned NE-SW. The large ranges in the concentrations of incompatible trace elements of SFF-1 indicate efficient differentiation processes in the crustal chambers leading from trachytes to peralkaline rhyolites. An estimate of the extent of differentiation made using Zr as fractionation index due to its high incompatibility in peralkaline rocks indicates formation of the peralkaline rhyolite by 60% fractional crystallization starting from the trachytic melts. No mafic activity has been observed for the first phase meaning that the basic magmas could have remained at depth, unerupted, as suggested for some MER volcanoes (Peccerillo et al. 2003; Hutchison et al. 2016), or could be mostly covered by later activity and thus difficult to identify and distinguish from the later mafic products. It is also possible that the compositions of the mafic products of the second phase represent the parental magma of the stratovolcano felsic products, erupted after the first phase and away from the stratovolcano. Since the stratovolcano is now heavily eroded and currently lacks any significant seismic activity, we suggest that it is now dormant or extinct.

During the second phase, both mafic and felsic magmas were erupted. The mafic magma storage depths range from ~ 9 to ~ 24 km, and the presence of reversed zoning in clinopyroxene, plagioclase and olivine crystals (online resource Table 3; online resource Fig. 3c) suggest a stacked plumbing system where the mafic magmas undergo differentiation by fractional crystallization and magma mixing. In addition, connections between the mafic and felsic feeding systems of the second phase are revealed by evidence of interaction between basalts and felsic magmas, indicated by the presence of two populations of clinopyroxene in the mafic lavas erupted nearby the sialic centres (as a whole Wo_{41-48} Fs_{9-32}). This suggests that the mafic magmas encountered mush-like felsic pockets during ascent and captured high Fs clinopyroxene without other clear evidence of magma mixing. The felsic products of the second phase (0.12 Ma from Barberi et al. 1972) are mostly aphyric and effusive, systematically more evolved (except for G33) and more peralkaline compared to the stratovolcano products and occupy a very narrow chemical range. It is possible that these aphyric and acidic lavas originated from highly fractionated melts rising from a relatively deep reservoir slowly enough to allow efficient gas/melt decoupling, preventing explosive activity (Gonnermann and Manga 2007); efficient crystal-melt separation in the magma chamber or adiabatic decompression-induced crystal resorption may explain the aphyric texture. This phase is characterized by the development of structures parallel to the NNW-SSE Red Sea trend and a shift in activity to the western side of the stratovolcano, where the youngest structures including RMF-4, FFD-4 and cinder cones occur. The youngest volcanism and structures correlate spatially with the majority of the recent seismicity, suggesting that this region is the current locus of strain and magmatism. We also interpret that the seismicity at the southern end of the MVF is caused by faulting on NNW-SSE planes along the rift axis, as short en-echelon faults are mapped across a ~ 10-km-wide axial zone (Fig. 8). En-echelon faults can also feed fissure eruptions during episodes of magma migration.

The marked changes in the types of erupted products, the different magma chamber depths, the distribution of the recent seismic activity and the structural arrangement between the two evolutionary phases of the MVF show that the recent activity of MVF differs from the first phase and it is now typical of an active magmatic rift segment.

A petrogenetic discussion of the magmatic evolution of MVF was not the focus of this work due to lack of mafic and intermediate products and of a complete sampling coverage of the area. We are aware that new studies on the stratovolcano, and in particular on the associated mafic products if outcropping, are needed to test our geochemical and petrological interpretation. Nevertheless, a process of fractional crystallization from transitional basalts to rhyolite, similar to those described for Dabbahu volcano (Barberi et al. 1975; Field et al. 2013), can be envisaged for the MVF products, with FFD-4 as a whole reaching a higher extent of differentiation with respect to SFF-1. We also show differences in Sr and Ba for the same degree of evolution (Zr or Th content) indicating differences in the fractionation process between the two felsic phases. We therefore speculate that the described chemical differences, in particular the different trace element ratios of felsic rocks between the two phases (Sr and Ba; Fig. 6b) are not only due to different degrees of fractional crystallization but also due to major differences in the evolutionary processes. The major differences in the evolutionary processes are possibly linked to different P–T-H_2O conditions of magma storage or variable extent of crustal assimilation that combined with the differences regarding the erupted products and the geobarometric estimates could be related to differences in the plumbing system architecture.

The MVF magma source and comparison to other rift volcanoes

Taken as a whole, the MVF products show a similar distribution of major and trace elements to Dabbahu volcano, except for the G33 lavas of the stratovolcano summit, reaching very high incompatible element contents (Fig. 6; online resource Figs. 7 and 8). In particular, the RMF-4 phase of MVF and the on-axis volcanism of Dabbahu volcano (Field et al. 2013) are both characterized by eruption of a significant volume of transitional mafic magmas. The recent mafic flows, just like at Dabbahu volcano, are associated with aphyric and obsidian-rich comendite erupted from several scattered vents and producing small volume domes or lava flows.

Lithosphere thinning is an important process influencing the depth of partial melting in the rising asthenosphere beneath rift systems. The across- and along-rift variation in the extent of stretching and thinning of the lithosphere leads to partial melting by decompression at different depths and consequently to different geochemical composition of the basaltic melts (Rooney 2010). We compared the chemical composition of the MVF mafic products (MgO wt% > 4) to similar mafic rocks of other Afar volcanoes by means of rare earth element ratios (Fig. 9). We use the La/Sm ratio to

evaluate the degree of partial melting and/or source enrichment and the ratio Tb/Yb for the depth of the melting column (Rooney 2010; Wang et al. 2002). In fact, magmas generated at a depth sufficient to have residual garnet in the source show a marked fractionation in the middle and heavy rare earth elements (e.g. Tb/Yb, Dy/Yb; Wang et al. 2002). High pressure clinopyroxene of a spinel lherzolite source behaves somewhat like garnet, but with much lower effect (Rooney 2010).

We considered the marginal Nabro volcano (Donovan et al. 2018) and the transverse Assab range (Teklay et al. 2010), the on-axis Dabbahu volcano (Barberi et al. 1975; Hoare et al. 2020), the Badi volcano in the Dabbahu segment (Ferguson et al. 2013), the products from the Dabbahu and Manda Hararo segments (Ferguson et al. 2013; Barrat et al. 2003) and the Erta Ale (Barrat et al. 1998) magmatic segment fissural products. As a whole, the mafic products of these volcanic centres range from 0.8 to 3.8 in La_N/Sm_N and from 1.0 to 2.2 in Tb_N/Yb_N (Fig. 9), crossing the Tb_N/Yb_N values at the transition between the spinel- and the garnet-bearing mantle sources derived from magma modelling in the Basin and Range province (Wang et al. 2002). Contributions from melting a garnet-bearing lower crust can be ruled out due to the low crustal thickness,
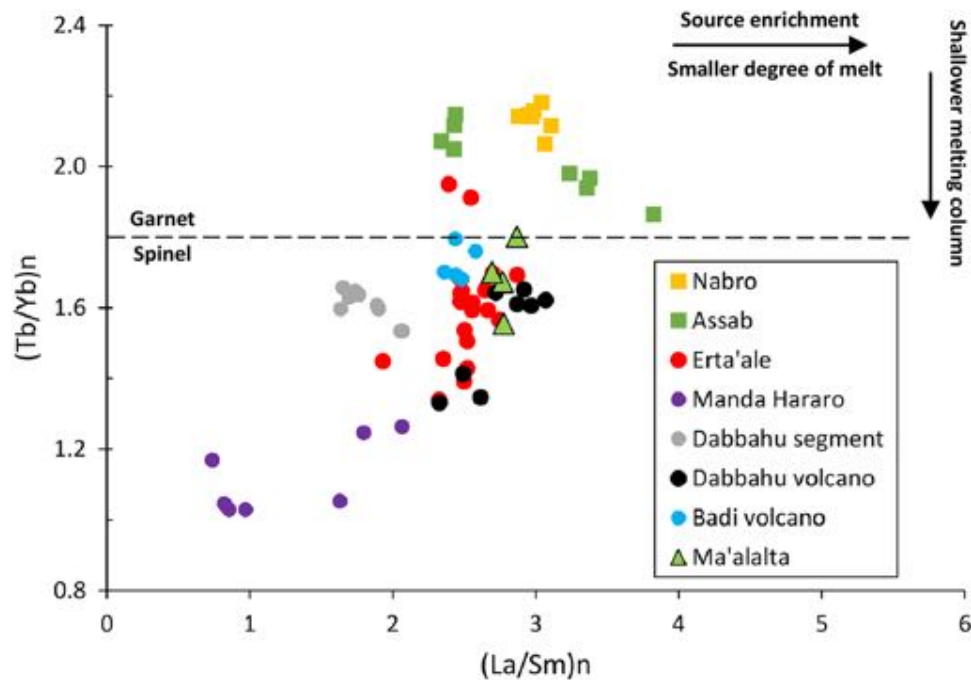

Fig. 9 Plot of Tb/Yb and La/Sm normalized to chondritic values (McDonough and Sun 1995). Only samples with MgO greater than 4 wt% are plotted. The division between spinel and garnet-dominated melting is derived from magma modelling in the Basin and Range province (Wang et al. 2002). As a comparison with the MVF, volcanism of different locations of the Afar region is shown: the marginal Nabro volcano (Donovan et al. 2018) and the transverse Assab range

(Teklay et al. 2010), the on-axis Dabbahu volcano (Barberi et al. 1975; Hoare et al. 2020), the Badi volcano in the Dabbahu segment (Ferguson et al. 2013), the products from the Dabbahu and Manda Hararo segments (Ferguson et al. 2013; Barrat et al. 2003) and Erta Ale (Barrat et al. 1998) rift axis fissural products. See text for explanation

ranging from 15 km beneath the Danakil Depression to 25–30 km beneath the Danakil microplate (Hammond et al. 2011). The fractionation of garnet under water-saturated conditions observed in some arc settings (Alonso-Perez et al. 2009) can also be excluded given the lack of hydrous phases in Afar mafic volcanism. Therefore, we interpret the variation in Tb_N/Yb_N as the result of changes in the melting column depth due to variations in lithospheric thickness. The marginal volcanism (i.e. Nabro and Assab range) is related to a deeper, garnet-bearing source ($Tb_N/Yb_N > 1.8$), while the MVF is similar to the axial volcanism (i.e. Badi volcano, Dabbahu volcano, Dabbahu and Manda Hararo segments and Erta Ale) and is related to a shallower source ($Tb_N/Yb_N < 1.8$, spinel lherzolite in the Wang et al. 2002 model for Basin and Range, while still in the garnet stability field according to Ferguson et al. (2013)). This difference is in agreement with the more evolved rifting stage (and thinner lithosphere) of the axial magmatic segments and strengthens the analogy between MVF recent volcanism and axial volcanism.

Therefore, we suggest that the geochemistry of the available mafic samples of the MVF, consistent with the other observations of this work, may be taken as an indication that the recent phase of the MVF is more typical of the axial volcanism. Additional work specifically on the MVF mafic rocks is necessary to fully define the mantle sources and melting conditions. However, based on several different lines of evidence from volcanology, geochemistry, seismicity and petrology, we propose that MVF evolved from an initial felsic central stratovolcano to an active magmatic segment.

Strain and magmatism are generally thought to progressively localize in-rift to narrow magmatic segments and the rift margin being progressively abandoned during magma-rich rifting (Hayward and Ebinger 1996; Wolfenden et al. 2005). However, here we have presented evidence of a young axial segment close to the rift margin of Afar (Fig. 1 and Fig. 3), suggesting that the process of strain localization may be more complex. Studies from Iceland suggest that rift zones can initiate as several subparallel overlapping rifts during incipient rifting. Some zones do not fully evolve like the Öræfajökull–Snæfell volcanic flank zone which initially developed on a preexisting cross-rift structure and then was abandoned (Hards et al. 2000). On the other hand, subparallel overlapping rifts can be active at the same time in response to the plate migration with respect to a stable plume, like the Eastern and Western volcanic zones (LaFemina et al. 2005). Using this analogy, the origin of MVF could be linked to a pre-existing lithospheric weakness guiding where strain localizes (e.g. Muirhead and Kattenhorn 2018) or to the interaction between the plate boundary and a hotspot.

Conclusions

In this paper, we integrate volcanological, geochemical, petrological and seismic data for the Ma'Alalta volcanic field, near the western margin of Afar, and we present a new geological map coupled with geochemical and petrological analyses. Growth of the MVF started at around 0.55 Ma with the building of a stratovolcano, later modified by caldera-forming explosive eruptions and by effusion of silicic intracaldera domes. The volcanic structures indicate a NE-SW (across-rift) trending tectonic regime in this first phase. In contrast, the recent volcanic activity of MVF shifted towards mafic lava fields, cinder cones and peralkaline obsidian-rich silicic domes erupted from several vents aligned NNW-SSE, parallel to the Red Sea rift. Inferred magma storage depths from mineral geobarometry suggest a shallow chamber at ~5 km below the silicic stratovolcano, while a stacked plumbing system with polybaric magma storage levels between ~9 and ~24 km depth fed the recent basalts. The geochemical and petrographic features indicate distinct plumbing systems and differentiation paths of felsic magmas between the early (stratovolcano) and recent volcanic phases. The recent NNW-SSE-trending mafic rocks geochemical features are similar to the nearby Dabbahu and Badi volcanoes and differ from marginal activity. The pattern of volcanism and recent seismicity defines a ~35-km-long magmatic segment. We interpret the wide set of observations as evidence that the activity at the MVF evolved from a felsic central stratovolcano to an active rift segment, showing that localised axial extension can be heavily offset towards the rift margin.

Data availability The authors confirm that the data supporting the findings of this study are available within the article and its supplementary materials.

Code availability Not applicable.

Declarations

Conflict of interest The authors declare no competing interests.

References

Alonso-Perez R, Müntener O, Ulmer P (2009) Igneous garnet and amphibole fractionation in the roots of island arcs: experimental constraints on andesitic liquids. Contrib Mineral Petrol 157:541–558. https://doi.org/10.1007/s00410-008-0351-8

Barberi F, Santacroce R (1980) The Afar Stratoid Series and the magmatic evolution of East African rift system. Bull Soc Géol France S7-XXII (6):891–899. https://doi.org/10.2113/gssgfbull.s7-xxii.6.891

Barberi F, Borsi S, Ferrara G, Marinelli G, Varet J (1970) A discussion on the structure and evolution of the Red Sea and the nature of the Red Sea, Gulf of Aden and Ethiopia rift junction - relations between tectonics and magmatology in the northern Danakil depression (Ethiopia). Philos Tr R S-A 267:293–311. https://doi.org/10.1098/rsta.1970.0037

Barberi F, Borsi S, Ferrara G, Marinelli G, Santacroce R, Tazieff H, Varet J (1972) Evolution of the Danakil Depression (Afar, Ethiopia) in Light of Radiometric Age Determinations. The J Geol 80:720–729. https://doi.org/10.1086/627797

Barberi F, Bonatti E, Marinelli G, Varet J (1974a) Transverse tectonics during the split of a continent: data from the Afar rift. Tectonophysics 23:17–29. https://doi.org/10.1016/0040-1951(74)90108-5

Barberi F, Santacroce R, Varet J (1974b) Silicic peralkaline volcanic rocks of the Afar depression (Ethiopia). Bulletin Volcanologique 38:755–790. https://doi.org/10.1007/bf02596907

Barberi F, Ferrara G, Santacroce R, Treuil M, Varet J (1975) A transitional Basalt-Pantellerite Sequence of fractional crystallization, the Boina Centre (Afar Rift, Ethiopia). J Petrol 16:22–56. https://doi.org/10.1093/petrology/16.1.22

Barrat J, Fourcade S, Jahn B, Cheminée J, Capdevila R (1998) Isotope (Sr, Nd, Pb, O) and trace-element geochemistry of volcanics from the Erta'Ale range (Ethiopia). J Volcanol Geotherm Res 80:85–100. https://doi.org/10.1016/s0377-0273(97)00016-4

Barrat J, Joron J, Taylor R, Fourcade S, Nesbitt R, Jahn B (2003) Geochemistry of basalts from Manda Hararo, Ethiopia: LREE-depleted basalts in Central Afar. Lithos 69:1–13. https://doi.org/10.1016/s0024-4937(03)00044-6

Belachew M, Ebinger C, Coté D, Keir D, Rowland J, Hammond J, Ayele A (2011) Comparison of dike intrusions in an incipient seafloor-spreading segment in Afar, Ethiopia: seismicity perspectives. J Geophys Res. https://doi.org/10.1029/2010jb007908

Best MG (2013) Igneous and metamorphic petrology. John Wiley & Sons

Civetta L, de Fino M, Gasparini P, Ghiara M, La Volpe L, Lirer L (1975) Structural meaning of East-Central Afar volcanism (Ethiopia, T.F.A.I.). The J Geol 83:363–373. https://doi.org/10.1086/628098

De Fino M, Volpe L, Lirer L (1978) Geology and volcanology of the Edd-Bahar Assoli area (Ethiopia). Bulletin Volcanologique 41:32–42. https://doi.org/10.1007/bf02597681

Donovan A, Blundy J, Oppenheimer C, Buisman I (2018) The 2011 eruption of Nabro volcano, Eritrea: perspectives on magmatic processes from melt inclusions. Contrib Mineral Petrol 173:1–23. https://doi.org/10.1007/s00410-017-1425-2

Ebinger CJ, Keir D, Ayele A, Calais E, Wright TJ, Belachew M, Hammond JO, Campbell E, Buck WR (2008) Capturing magma intrusion and faulting processes during continental rupture: seismicity of the Dabbahu (Afar) rift. Geophys J Int 174(3):1138–1152. https://doi.org/10.1111/j.1365-246X.2008.03877.x

Ferguson DJ, Barnie TD, Pyle DM, Oppenheimer C, Yirgu G, Lewi E, Kidane T, Carn S, Hamling I (2010) Recent rift-related volcanism in Afar. Ethiopia Earth Planet Sci Lett 292(3–4):409–418. https://doi.org/10.1016/j.epsl.2010.02.010

Ferguson DJ, Maclennan J, Bastow ID, Pyle D, Jones SM, Keir D, Blundy JD, Plank T, Yirgu G (2013) Melting during late-stage rifting in Afar is hot and deep. Nature 499(7456):70–73. https://doi.org/10.1038/nature12292

Field L, Blundy J, Brooker RA, Wright T, Yirgu G (2012) Magma storage conditions beneath Dabbahu Volcano (Ethiopia) constrained by petrology, seismicity and satellite geodesy. Bull Volcanol 74(5):981–1004. https://doi.org/10.1007/s00445-012-0580-6

Field L, Blundy J, Calvert A, Yirgu G (2013) Magmatic history of Dabbahu, a composite volcano in the Afar Rift. Ethiopia Geol Soc Am Bull 125(1–2):128–147. https://doi.org/10.1130/B30560.1

Gonnermann HM, Manga M (2007) The fluid mechanics inside a volcano. Annu Rev Fluid Mech 39:321–356. https://doi.org/10.1146/annurev.fluid.39.050905.110207

Govindaraju K (1980) Report (1980) on three GIT-IWG rock reference samples: Anorthosite from Greenland, AN-G; Basalte d'Essey-la-Côte, BE-N; Granite de Beauvoir. MA-N Geostandard Newslett 4(1):49–138. https://doi.org/10.1111/j.1751-908X.1980.tb00274.x

Govindaraju K (1994) 1994 compilation of working values and sample description for 383 geostandards. Geostandard Newslett 18:1–158. https://doi.org/10.1046/j.1365-2494.1998.53202081.x-i1

Hagos M, Koeberl C, De Vries BVW (2016) The Quaternary volcanic rocks of the northern Afar Depression (northern Ethiopia): perspectives on petrology, geochemistry, and tectonics. J African Earth Sci 117:29–47. https://doi.org/10.1016/j.jafrearsci.2015.11.022

Hamlyn J, Wright T, Walters R, Pagli C, Sansosti E, Casu F, Pepe S, Edmonds M, Kilbride BM, Keir D, Neuberg J, Oppenheimer C (2018) What causes subsidence following the 2011 eruption at Nabro (Eritrea). Progr Earth Planet Sci 5(1):1–15. https://doi.org/10.1186/s40645-018-0186-5

Hammond JO, Kendall JM, Stuart GW, Keir D, Ebinger C, Ayele A, Belachew M (2011) The nature of the crust beneath the Afar triple junction: evidence from receiver functions. Geochem Geophys Geosy 12:Q12004. https://doi.org/10.1029/2011GC003738

Hards VL, Kempton PD, Thompson RN, Greenwood PB (2000) The magmatic evolution of the Snaefell volcanic centre; an example of volcanism during incipient rifting in Iceland. J Volcanol Geotherm Res 99(1–4):97–121. https://doi.org/10.1016/S0377-0273(00)00160-8

Hayward NJ, Ebinger CJ (1996) Variations in the along-axis segmentation of the Afar Rift system. Tectonics 15(2):244–257. https://doi.org/10.1029/95TC02292

Hoare L, Klaver M, Saji NS, Gillies J, Parkinson IJ, Lissenberg CJ, Millet MA (2020) Melt chemistry and redox conditions control titanium isotope fractionation during magmatic differentiation. Geochim Cosmochim Acta 282:38–54. https://doi.org/10.1016/j.gca.2020.05.015

Hofmann C, Courtillot V, Feraud G, Rochette P, Yirgu G, Ketefo E, Pik R (1997) Timing of the Ethiopian flood basalt event and implications for plume birth and global change. Nature 389(6653):838–841. https://doi.org/10.1038/39853

Hutchison W, Pyle DM, Mather TA, Yirgu G, Biggs J, Cohen BE, Barfod DN, Lewi E (2016) The eruptive history and magmatic evolution of Aluto volcano: new insights into silicic peralkaline volcanism in the Ethiopian rift. J Volcanol and Geoth Res 328:9–33. https://doi.org/10.1016/j.jvolgeores.2016.09.010

Hutchison W, Mather TA, Pyle DM, Boyce AJ, Gleeson ML, Yirgu G, Blundy JD, Ferguson DJ, Vye-Brown C, Millar IL, Sims KW, Finch AA (2018) The evolution of magma during continental rifting: new constraints from the isotopic and trace element signatures of silicic magmas from Ethiopian volcanoes. Earth Planet Sc Lett 489:203–218. https://doi.org/10.1016/j.epsl.2018.02.027Get

Illsley-Kemp F, Keir D, Bull JM, Gernon TM, Ebinger C, Ayele A, Hammond O, Kendall JM, Goitom B, Belachew M (2018) Seismicity during continental breakup in the Red Sea rift of northern Afar. J Geophys Res Solid Earth 123(3):2345–2362. https://doi.org/10.1002/2017JB014902

Kidane T, Courtillot V, Manighetti I, Audin L, Lahitte P, Quidelleur X, Gillot PY, Gallet Y, Carlut J, Haile T (2003) New paleomagnetic and geochronologic results from Ethiopian Afar: block rotations linked to rift overlap and propagation and determination of a~ 2 Ma reference pole for stable Africa. J Geophys Res: Solid Earth 108:2102. https://doi.org/10.1029/2001JB000645

Kieffer B, Arndt N, Lapierre H, Bastien F, Bosch D, Pecher A, Yirgu G, Ayalew D, Weis D, Jerram DA, Keller F, Meugniot C (2004) Flood and shield basalts from Ethiopia: magmas from the African superswell. J Petrol 45(4):793–834. https://doi.org/10.1093/petrology/egg112

LaFemina PC, Dixon TH, Malservisi R, Árnadóttir T, Sturkell E, Sigmundsson F, Einarsson P (2005) Geodetic GPS measurements in south Iceland: strain accumulation and partitioning in a propagating ridge system. J Geophys Res: Solid Earth 110:B11405. https://doi.org/10.1029/2005JB003675

Marty B, Gezahegn Y (1996) Helium isotopic variations in Ethiopian plume lavas: nature of magmatic sources and limit on lower mantle contribution. Earth Planet Sci Lett 144(1–2):223–237. https://doi.org/10.1016/0012-821X(96)00158-6

Masotta M, Mollo S, Freda C, Gaeta M, Moore G (2013) Clinopyroxene-liquid thermometers and barometers specific to alkaline differentiated magmas. Contrib Mineral Petrol 166(6):1545–1561. https://doi.org/10.1007/s00410-013-0927-9

McClusky S, Reilinger R, Ogubazghi G, Amleson A, Healeb B, Vernant P, Sholan J, Fisseha S, Asfaw L, Bendick R, Kogan L (2010) Kinematics of the southern Red Sea-Afar Triple Junction and implications for plate dynamics. Geophys Res Lett 37:L05301. https://doi.org/10.1029/2009GL041127

McDonough WF, Sun SS (1995) The composition of the earth. Chem Geol 120(3–4):223–253. https://doi.org/10.1016/0009-2541(94)00140-4

Medynski S, Pik R, Burnard P, Williams A, Vye-Brown C, Ferguson D, Blard PH, France L, Yirgu G, Seid JI, Ayalew D, Calvert A (2013) Controls on magmatic cycles and development of rift topography of the Manda Hararo segment (Afar, Ethiopia): insights from cosmogenic 3He investigation of landscape evolution. Earth Planet Sci Lett 367:133–145. https://doi.org/10.1016/j.epsl.2013.02.006

Medynski S, Pik R, Burnard P, Vye-Brown C, France L, Schimmelpfennig I, Whaler K, Johnson N, Benedetti L, Ayalew D, Yirgu G (2015) Stability of rift axis magma reservoirs: spatial and temporal evolution of magma supply in the Dabbahu rift segment (Afar, Ethiopia) over the past 30 kyr. Earth Planet Sci Lett 409:278–289. https://doi.org/10.1016/j.epsl.2014.11.002

Medynski S, Pik R, Burnard P, Dumont S, Grandin R, Williams A, Blard PH, Schimmelpfennig I, Vye-Brown C, France L, Ayalew D, Benedetti L, Yirgu G, ASTER team (2016) Magmatic cycles pace tectonic and morphological expression of rifting (Afar depression, Ethiopia). Earth Planet Sci Lett 446:77–88. https://doi.org/10.1016/j.epsl.2016.04.014

Muirhead JD, Kattenhorn SA (2018) Activation of preexisting transverse structures in an evolving magmatic rift in East Africa. J Structural Geol 106:1–18. https://doi.org/10.1016/j.jsg.2017.11.004

Neave DA, Putirka KD (2017) A new clinopyroxene-liquid barometer, and implications for magma storage pressures under Icelandic rift zones. Am Mineral 102(4):777–794. https://doi.org/10.2138/am-2017-5968

Oppenheimer C, Francis P (1998) Implications of longeval lava lakes for geomorphological and plutonic processes at Erta'Ale volcano. Afar J Volcanol Geotherm Res 80(1–2):101–111. https://doi.org/10.1016/S0377-0273(97)00041-3

Oppenheimer C, Khalidi L, Gratuze B, Iverson N, Lane C, Vidal C, Sahle Y, Blegen N, Yohannes E, Donovan A, Goitom B, Hammond JOS, Keall E, Ogubazghi G, Mclntosh B, Büntgen U (2019) Risk and reward: explosive eruptions and obsidian lithic resource at Nabro volcano (Eritrea). Quaternary Sci Rev 226:105995. https://doi.org/10.1016/j.quascirev.2019.105995

Peccerillo A, Barberio MR, Yirgu G, Ayalew D, Barbieri M, Wu TW (2003) Relationships between mafic and peralkaline silicic magmatism in continental rift settings: a petrological, geochemical and isotopic study of the Gedemsa volcano, central Ethiopian rift. J Petrol 44(11):2003–2032. https://doi.org/10.1093/petrology/egg068

Pik R, Deniel C, Coulon C, Yirgu G, Marty B (1999) Isotopic and trace element signatures of Ethiopian flood basalts: evidence for plume–lithosphere interactions. Geochim Cosmochim Acta 63(15):2263–2279. https://doi.org/10.1016/S0016-7037(99)00141-6

Putirka KD (2008) Thermometers and barometers for volcanic systems. Rev Mineral Geochem 69(1):61–120. https://doi.org/10.2138/rmg.2008.69.3

Rooney TO (2010) Geochemical evidence of lithospheric thinning in the southern Main Ethiopian Rift. Lithos 117(1–4):33–48. https://doi.org/10.1016/j.lithos.2010.02.002

Stab M, Bellahsen N, Pik R, Quidelleur X, Ayalew D, Leroy S (2016) Modes of rifting in magma-rich settings: tectono-magmatic evolution of Central Afar. Tectonics 35(1):2–38. https://doi.org/10.1002/2015TC003893

Tazieff H, Marinelli G, Barberi F, Varet J (1969) Géologie de l'Afar septentrional. Bulletin Volcanologique 33(4):1039–1072. https://doi.org/10.1007/BF02597707

Teklay M, Scherer EE, Mezger K, Danyushevsky L (2010) Geochemical characteristics and Sr–Nd–Hf isotope compositions of mantle xenoliths and host basalts from Assab, Eritrea: implications for the composition and thermal structure of the lithosphere beneath the Afar Depression. Contrib Mineral Petrol 159(5):731–751. https://doi.org/10.1007/s00410-009-0451-0

Varet J (1978) Geological Map of Central and Southern Afar (Ethiopia and Djibouti Republic). CHRS

Wang K, Plank T, Walker JD, Smith EI (2002) A mantle melting profile across the Basin and Range, SW USA. J Geophys Res 107:ECV 5 1-21. https://doi.org/10.1029/2001JB000209

Wiart P, Oppenheimer C (2005) Large magnitude silicic volcanism in north Afar: the Nabro Volcanic Range and Ma'alalta volcano. Bull Volcanol 67(2):99–115. https://doi.org/10.1007/s00445-004-0362-x

Wolfenden E, Ebinger C, Yirgu G, Renne PR, Kelley SP (2005) Evolution of a volcanic rifted margin: Southern Red Sea. Ethiopia Geol Soc Am Bull 117(7–8):846–864. https://doi.org/10.1130/B25516.1

Wright TJ, Ebinger C, Biggs J, Ayele A, Yirgu G, Keir D, Stork A (2006) Magma-maintained rift segmentation at continental rupture in the 2005 Afar dyking episode. Nature 442(7100):291–294. https://doi.org/10.1038/nature04978

Wright TJ, Sigmundsson F, Pagli C, Belachew M, Hamling IJ, Brandsdóttir B, Keir D, Pedersen R, Ayele A, Ebinger C, Einarsson P, Lewi E, Calais E (2012) Geophysical constraints on the dynamics of spreading centres from rifting episodes on land. Nat Geosci 5(4):242–250. https://doi.org/10.1038/ngeo1428

Zumbo V, Féraud G, Bertrand H, Chazot G (1995) 40Ar39Ar chronology of Tertiary magmatic activity in southern Yemen during the early Red Sea-Aden rifting. J Volcanol Geotherm Res 65(3–4):265–279. https://doi.org/10.1016/0377-0273(94)00106-Q